Experimental Visualization of Hybrid Combustion: Results at Elevated Pressures

Elizabeth T. Jens,* Ashley C. Karp,† Victor A. Miller,‡ G. Scott Hubbard,§ and Brian J. Cantwell¶
Stanford University, Stanford, California 94305

https://doi.org/10.2514/1.B37416

This work was undertaken in an effort to improve the understanding of the combustion processes inside classical and fast-burning hybrid rocket motors. In this paper, a combustion visualization experiment and various optics were used to explore the mass transfer phenomena, boundary-layer growth rates, and the flame location above combusting fuels at atmospheric and elevated chamber pressures. The results presented provide strong confirmation of the basic droplet formation and entrainment mechanism for fast-burning fuels at operating conditions representative of those in a typical hybrid rocket motor. Entrained filament structures were not observed to be the dominant feature at chamber pressures above the critical pressure of the fuel; instead, at high pressures, numerous intense mass ejection events emitting large numbers of droplets were observed to be a major mass transfer mechanism. Imaging diagnostics were successfully used to quantify the location of the flame and the boundary-layer edge for classical and high-regression-rate fuels at a range of operating conditions. The imaging systems are also used in conjunction with chamber pressure data to examine the flameholding instability around the leading edge of the fuel grain.

Nomenclature

a_l = absorption coefficient of the liquid, m^{-1}
B = blowing parameter
C = specific heat, $J/(kg \cdot K)$
C_f = skin-friction coefficient
C_H = Stanton number with blowing
C_{H0} = Stanton number without blowing
e = property at edge of boundary layer
Fr = correction factor for surface roughness
G = total mass flux, $kg/(m^2 \cdot s)$
H = melt layer thickness, m
h_e = total heat of entrainment, J/kg
h_m = total heat of melting, J/kg
h_v = total effective heat of gasification, J/kg
L_m = latent heat of melting, J/kg
L_v = latent heat of vaporization, J/kg
$\dot{m}_{\text{ent}}$ = entrained mass flow rate per unit area, $kg/(m^2 \cdot s)$
P_d = dynamic pressure, Pa
$\dot{Q}_c$ = convective heat transfer at the fuel surface, $J/(m^2 \cdot s)$
$\dot{Q}_r$ = radiative heat transfer at the fuel surface, $J/(m^2 \cdot s)$
$\dot{r}$ = regression rate, m/s
$\dot{r}_{\text{ent}}$ = regression rate of fuel from entrainment mechanism, m/s
$\dot{r}_v$ = regression rate of fuel from vaporization, m/s
T_a = initial fuel temperature, K
T_g = average gas phase temperature, K
T_m = melting temperature, K
T_v = vaporization temperature, K
u = axial velocity, m/s
v = radial velocity, m/s
w = property at wall (fuel surface)
δ_l = characteristic thermal thickness in the liquid phase, m
ρ = density, kg/m^3
σ = surface tension, N/m

Presented as Paper 2014-3848 at the 50th AIAA/ASME/SAE/ASEE Joint Propulsion Conference, Cleveland, OH, 28–30 July 2014; received 19 November 2018; revision received 31 July 2019; accepted for publication 1 August 2019; published online 21 October 2019.

*Currently Propulsion Engineer, Propulsion and Fluid Flight Systems Group, Jet Propulsion Laboratory, California Institute of Technology, 4800 Oak Grove Drive, Pasadena, California 91109. Member AIAA.

†Currently Technologist, Propulsion and Fluid Flight Systems Group, Jet Propulsion Laboratory, California Institute of Technology, 4800 Oak Grove Drive, Pasadena, California 91109. Member AIAA.

‡Currently Vice President of Technology, SeekOps, Inc., 6101 W. Courtyard Drive, Building 5, Suite 100, Austin, Texas 78730.

§Professor–Adjunct, Department of Aeronautics and Astronautics, 496 Lomita Mall, Durand Building Room 363. Honorary Fellow AIAA.

¶Edward C. Wells Professor, Department of Aeronautics and Astronautics, 496 Lomita Mall, Durand Building Room 379. Fellow AIAA.

I. Introduction

THE adoption of hybrid motors for applications requiring large thrust has been inhibited by performance issues stemming from the use of slow-burning low-regression-rate fuels. The combustion of classical hybrid fuels is limited by low rates of melting, evaporation, and molecular diffusion. Efforts to increase the regression rate of classical fuels through increased heat transfer to the grain have seen only limited success [1], largely due to the blocking effect. Thus, in order to achieve large enough fuel mass flow rates to generate sufficient thrust for most applications, complicated multiport fuel grain designs are used to increase the burning surface area. Multiport fuel grains have inherently low volumetric loading. These grains also do not burn evenly, and combustion must be terminated as soon as one port is close to a burnthrough. Thus, these fuel grains tend to have large unburned sliver fractions and are susceptible to chunking. These issues have inhibited hybrid rocket adoption, despite their potential cost savings and reduced susceptibility to explosive failure. Such was the state of the art until 1997, when Karabeyoglu et al. discovered a class of high-regression-rate fuels in normal-alkane hydrocarbons with carbon numbers greater than approximately 14 [2]. These fuels, which include paraffin waxes, have demonstrated regression rates of approximately three to four times those of classical hybrids [2]. This high regression rate facilitates the use of a single circular port fuel grain, and thereby overcomes many of the problems that have plagued classical hybrid motors. Paraffin-based hybrid rockets now present a competitive alternative to conventional propulsion systems for many exploration missions [3–7].

Karabeyoglu et al. first proposed the mechanism for the increased regression rate of paraffin-based hybrid rockets in 2001 [2]; this mechanism is shown schematically in Fig. 1. They surmised that a thin liquid layer with low viscosity and surface tension is produced on the surface of high-regression-rate fuels as they burn. This liquid layer is unstable under the shear forces associated with the oxidizer gas flow in the port. This results in the entrainment of droplets into the gas stream, leading to a substantial increase in the fuel regression rate. The droplet entrainment mechanism effectively acts like a fuel spray injection system along the length of the motor, with increased surface area for mixing and reduced sensitivity to the blocking effect.

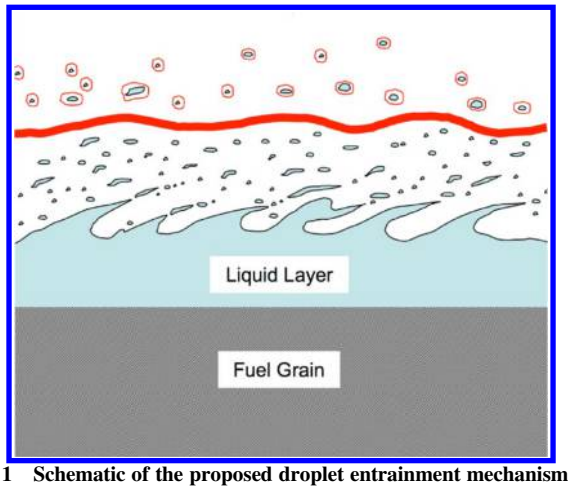

Fig. 1 Schematic of the proposed droplet entrainment mechanism for liquefying high-regression-rate fuels, originally reported by Karabeyoglu et al. in Ref. [2].

The rate at which fuel is entrained from the liquid layer was evaluated by Karabeyoglu et al. [2] using experimental results from Gater and L'Ecuyer [8], the linear stability theory, and theoretical studies of entrainment from the nuclear reactor field [9]. They proposed that the entrainment rate is strongly dependent on the viscosity of the melt layer μ, as well as on the thickness of the melt layer H, the dynamic pressure P_d, and the surface tension σ according to Eq. (1):

$$\dot{m}_{\text{ent}} \propto \frac{P_d^{\alpha} H^{\beta}}{\mu_l^{\varphi} \sigma^{\phi}} \tag{1}$$

Here, α, β, φ, and ϕ are all estimated to be in the range of one to two.

The classical hybrid rocket combustion theory detailed in Refs. [10–12] required modification in order to be applied to liquefying high-regression-rate fuels. In Ref. [9], Karabeyoglu et al. proposed three modifications to the existing theory for classical fuels. First, the effective heat of gasification that appears in the thermal blowing parameter is reduced because less energy is now required for fuel evaporation due to mass transfer as a result of mechanical entrainment of the liquid. Second, the presence of droplets between the fuel surface and the diffusion flame corresponds to a two-phase flow regime. Karabeyoglu et al. neglected the effect of the fuel droplets on the momentum and energy transfer between the flame and the fuel surface, and thus wrote the blocking factor in terms of only the gas phase mass transfer from the fuel surface [Eq. (2)]:

$$C_H / C_{H0} = f(B_g) \tag{2}$$

Note that the blowing parameter B is defined according to Eq. (3); the subscript g is used to indicate that we are only using the gas phase properties:

$$B_g \equiv \left. \frac{2(\rho v)_w}{\rho_e u_e C_f} \right|_g \tag{3}$$

Finally, the roughness of the fuel surface and the heat transfer to the fuel from the flame front are increased as a result of the roll waves and ripples in the liquid layer.

With these modifications, the equations governing the combustion of hybrid rocket motors using liquefying fuels become the series of Eqs. (4–7). These four equations can be solved to calculate the total fuel regression rate as a function of location and mass flux. Equation (4) is the mathematical statement that the total regression rate $\dot{r}$ is simply the addition of the regression rate due to entrainment $\dot{r}_{\text{ent}}$ and the regression rate due to evaporation $\dot{r}_v$. Equation (5) is derived from conservation of energy using a control volume that spans the surface of the liquid layer. Here, x refers to the axial distance along the fuel port. C_H and C_{H0} are the Stanton numbers, i.e., the ratio of heat transferred to the fluid to the thermal capacity of the fluid with and without blowing, respectively. Equation (6) is an expression for the heat transfer roughness correction parameter Fr originally suggested by Gater and L'Ecuyer [8]. Equation (7) is derived from Eq. (1). The coefficient a_{ent} is not explicitly listed but is a function of the propellant properties and the average gas density in the combustion chamber. For simplicity, it is assumed that a_{ent} is a constant for a given propellant:

$$\dot{r} = \dot{r}_{\text{ent}} + \dot{r}_v \tag{4}$$

$$\dot{r}_v + \dot{r}_{\text{ent}} \left[\frac{h_m}{h_e + L_v} + \frac{C_l (T_v - T_m)}{h_e + L_v} \left(\frac{\dot{r}_v}{\dot{r}} \right) \right] = Fr \frac{0.03 \mu_g^{0.2}}{\rho_f} \left(1 + \frac{\dot{Q}_r}{\dot{Q}_c} \right) B \frac{C_H}{C_{H0}} G^{0.8} x^{-0.2} \tag{5}$$

$$Fr = 1 + \frac{14.1 \rho_g^{0.4}}{G^{0.8} (T_g / T_v)^{0.2}} \tag{6}$$

$$\dot{r}_{\text{ent}} = a_{\text{ent}} \frac{G^{2\alpha}}{\dot{r}^{\beta}} \tag{7}$$

Equations (4–7) were solved by Karabeyoglu et al. and are shown to predict the burn rate of liquefying fuels with reasonable accuracy; see Refs. [2,13]. Note that these equations indicate that the burn rate of these fuels is independent of combustion chamber pressure.

The discovery of high-regression-rate liquefying fuels for hybrid motors generated a renewed interest in visualization experiments; see Table A5 in the Appendix for a complete summary. It was predicted that the size and shape of the entrained droplets will decrease with increasing combustion chamber pressure and oxidizer mass flux [1]. Furthermore, as the combustion chamber pressure increases well above the critical pressure of paraffin, which is approximately 670 kPa (97 psi) [13], it was expected that the surface of the droplets will become indistinct, and the entrained flow may start to more closely resemble a filamentlike structure [14]. Typical motor configurations use combustion chamber pressures above the critical pressure of paraffin, and thus there is considerable interest in the entrainment mechanism at supercritical pressures. Wada et al. published visuals of the droplet entrainment mechanism of fast-burning fuels at such pressures [15]; however, their range of oxidizer mass flux was limited, and their published images are difficult to interpret. More recently, Petrarolo et al. started to explore the effect of pressure on the combustion of liquefying fuels with their visualization experiment [16]. They presented initial black and white images and observations of the combustion of a liquefying fuel at a supercritical chamber pressure but at low oxidizer mass fluxes.

The overarching goal of this work was to observe the combustion of classical and high-regression-rate fuels at elevated chamber pressures representative of those within a typical hybrid rocket motor, and thereby investigate the validity of the proposed droplet entrainment mechanism. Advanced optics were used to quantify the flame location within the boundary layer in order to explore how the presence of droplets might affect the main diffusion flame and the boundary-layer thickness.

This paper builds upon previous visualization experiment results by presenting color, schlieren, and OH* chemiluminescence images for the combustion of both a high-regression-rate fuel and a classical fuel with oxygen at a range of pressures and oxidizer mass fluxes, including at conditions representative of a typical hybrid motor.

II. Methodology

An apparatus to visualize the combustion of hybrid rocket fuels with gaseous oxygen has been designed and constructed at Stanford University. It comprises three main components: the feed system, the flow conditioning system, and the combustion chamber. The flow conditioning system and combustion chamber are shown in Fig. 2. The flow conditioning system delivers uniform freestream oxidizer flow to the combustion chamber. Fuel grains are suspended on a cantilevered support within the combustion chamber, which is designed with optical access from three vantage points. The design of

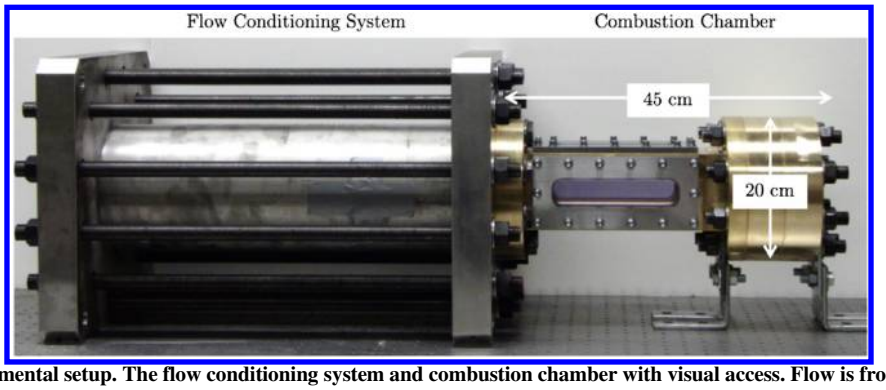

Fig. 2 Experimental setup. The flow conditioning system and combustion chamber with visual access. Flow is from left to right.

this combustion visualization experiment was discussed in detail in Refs. [17,18]. The tests presented in this paper were conducted at chamber pressures between 101.3 kPa (14.7 psi) and 1524.2 kPa (221.0 psi), and with oxidizer mass fluxes from 20.4 to 74.4 kg/(m$^2 \cdot$ s). The freestream unit Reynolds numbers (i.e., defined without imposing a characteristic length as $Re = \rho_e U_e/\mu_e$), ranged from 9.83×10^3 to 3.72×10^4 cm^{-1}. Freestream velocities ranged from 2.9 to 57.4 m/s. Table 1 provides an example of the variation in the fluid properties between the freestream and the location of combustion; these values were calculated using the data from test 34 and the chemical equilibrium with applications (CEA) program [19].

This paper is focused on test results that provide insight into the difference between the combustion of classical and high-regression-rate hybrid rocket fuels. Poly[methylmethacrylate] (PMMA), or $[C_5H_8O_2]_n$, test results are presented as representative results for classical fuels; and blackened paraffin (BP) wax, or $C_{32}H_{66}$, results are presented for representative high-regression-rate fuels. The paraffin fuel grains were made using FR5560 wax purchased from the Candlewic Company with 0.5% by mass addition of blackened dye (again from the Candlewic Company). PMMA was purchased from eStreet Plastics as a black Plexiglas® acrylic sheet. Details of the combustions of other fuels were provided in Refs. [17,18]. The main parameters for the tests, including camera settings, are provided in the Appendix (Tables A1–A4).

As discussed in the previous section, the location of the flame within the boundary layer is a key assumption in the analytic determination of the fuel regression rate for a given propellant combination. It was desired to investigate this, for both classical and high-regression-rate fuels, by attempting to quantify the location of the flame and the boundary-layer edge at a range of combustion chamber pressures. Schlieren imaging, using a Z-type schlieren configuration, was adopted to provide insight into the structure of the turbulent boundary layer above the fuel surface [18]. Schlieren images show density variations in the fluid flow. There is typically a sharp instantaneous demarcation surface between the turbulent and nonturbulent fluid for these flows [20], and thus the schlieren images were expected to provide clear images of the thermal boundary-layer edge. The location of the thermal boundary-layer edge for these flows should be roughly coincident with the edge of the momentum boundary layer; see the experimental results collected by Wooldridge and Muzzy [21] and Muzzy and Woolridge [22] for evidence of the validity of this statement. The location of the flame was evaluated using images of OH* chemiluminescence. OH* has been used to indicate the location of flame kernels, reactions, and the intensity of burning in a variety of studies [23,24]. Here, the OH* signal is interpreted simply as a marker of reaction. The justification for this statement and a discussion of the associated assumptions were provided in Ref. [25]. Details of the process used to overlay and quantify the schlieren and OH* chemiluminescence images were provided in Ref. [25]. It is worth noting that both of these imaging techniques generate path-integrated images.

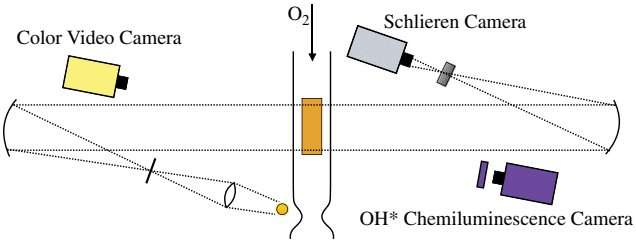

Fig. 3 Schematic of the top-down view of the combustion visualization facility showing the configuration of the color video, schlieren and OH* chemiluminescence optics. Note that the schlieren light source scale is increased for visibility, the physical scale of the light emitting element is 5×5 mm.

The optics used for this work are shown schematically in Fig. 3. The schlieren system consists of an off-the-shelf light-emitting diode source; two 0.192 m (7.54 in.) diameter mirrors, each with a focal length of 1.435 m (56.5 in.); a knife edge; and a MotionPro X3 Plus camera with a 105 mm Nikon lens. The knife edge was oriented horizontally in order to better resolve vertical density gradients along the boundary-layer edge. The OH* chemiluminescence images were recorded on a Photron APX i^2 intensified camera, using a 105 mm Nikkor UV lens, and an Asahi Spectra high-transmission bandpass filter centered at 313 nm with a full-width half-maximum of 5 nm. The schlieren and OH* images were triggered together and recorded at the same frame rate. Details of the all of the camera settings are provided in the Appendix.

III. Qualitative Results and Observations

The droplet entrainment mechanism for fuel mass transfer was successfully visualized at a range of operating conditions. Of the three imaging methods employed, the color images most clearly show the droplet entrainment mechanism; see Figs. 4 and 5. The combustion of PMMA is included in Fig. 4 for contrast as a representative classical fuel.

Table 1 Example of fluid properties in the freestream and during combustion[a]

Parameter	T, K	μ, Pa·s	$\gamma = C_p/C_v$	Pr	$Re = \rho U/\mu$, cm^{-1}	ρ, kg/m^3
Freestream[b]	297	2.06×10^{-5}	1.40	0.71	2.66×10^4	16.09
Combustion	3466	1.1×10^{-5}	1.12	0.67	5.06×10^5	1.18

[a]Combustion values are determined from stoichiometric combustion of paraffin with oxygen, corresponding to an O/F ratio of 3.45, at 1379 kPa (200 psi) using Chemical Equilibrium with Applications [19]. The Prandtl number listed assumes frozen reactions. The Reynolds number is calculated using the free-stream velocity for Test 34.
[b]Listed numbers from test 34 data.

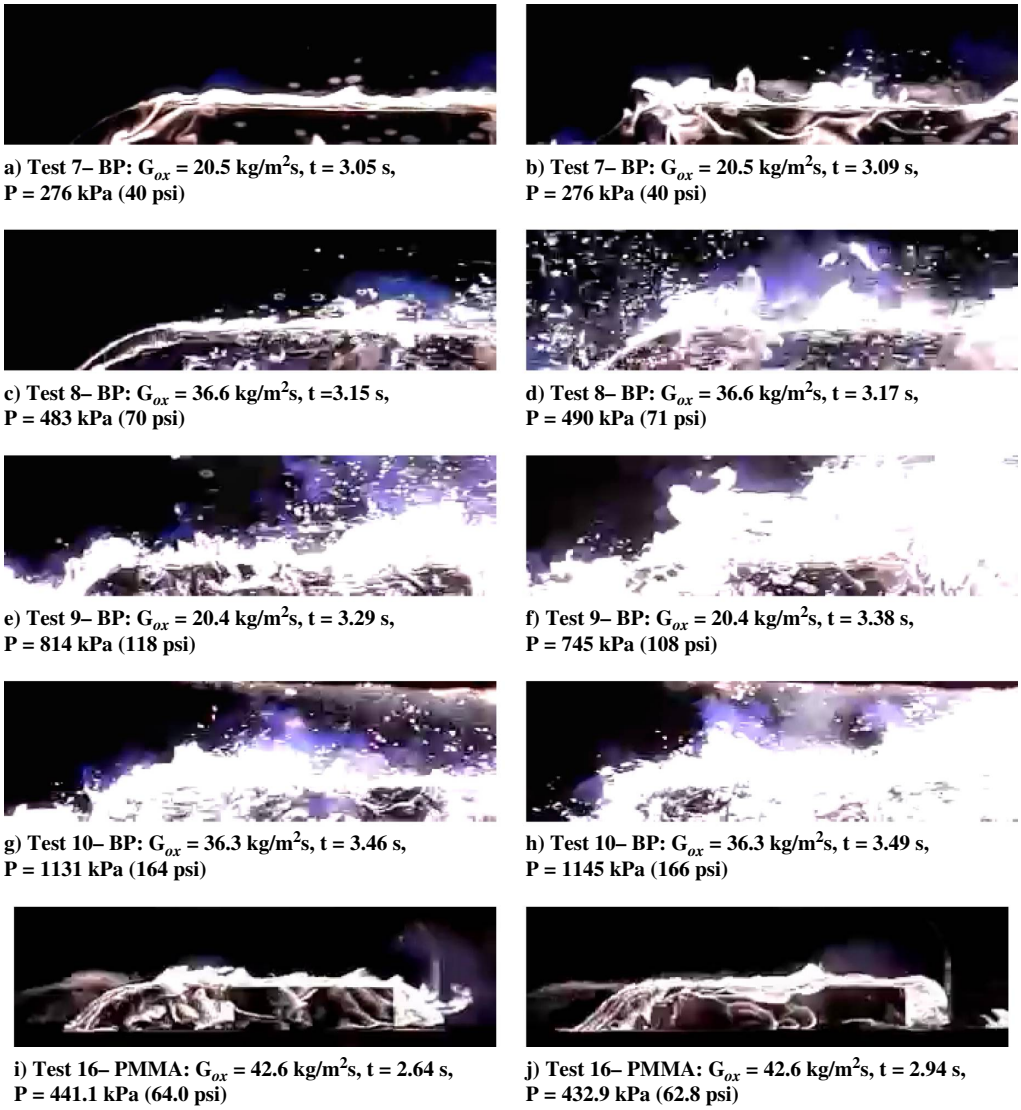

a) Test 7– BP: G_{ox} = 20.5 kg/m^{2}s, t = 3.05 s, P = 276 kPa (40 psi)

b) Test 7– BP: G_{ox} = 20.5 kg/m^{2}s, t = 3.09 s, P = 276 kPa (40 psi)

c) Test 8– BP: G_{ox} = 36.6 kg/m^{2}s, t =3.15 s, P = 483 kPa (70 psi)

d) Test 8– BP: G_{ox} = 36.6 kg/m^{2}s, t = 3.17 s, P = 490 kPa (71 psi)

e) Test 9– BP: G_{ox} = 20.4 kg/m^{2}s, t = 3.29 s, P = 814 kPa (118 psi)

f) Test 9– BP: G_{ox} = 20.4 kg/m^{2}s, t = 3.38 s, P = 745 kPa (108 psi)

g) Test 10– BP: G_{ox} = 36.3 kg/m^{2}s, t = 3.46 s, P = 1131 kPa (164 psi)

h) Test 10– BP: G_{ox} = 36.3 kg/m^{2}s, t = 3.49 s, P = 1145 kPa (166 psi)

i) Test 16– PMMA: G_{ox} = 42.6 kg/m^{2}s, t = 2.64 s, P = 441.1 kPa (64.0 psi)

j) Test 16– PMMA: G_{ox} = 42.6 kg/m^{2}s, t = 2.94 s, P = 432.9 kPa (62.8 psi)

Fig. 4 Color images of combustion of paraffin (BP) and PMMA. Oxidizer flow is from left to right. Images during nominal combustion (left) and intense mass ejection events (right). Times listed refer to time after ignition. Camera settings are in the Appendix.

The droplet entrainment mechanism for liquefying fuels was observed to change as the pressure increased from atmospheric pressure: through subcritical pressures up to pressures above the critical pressure of paraffin. Few droplets were seen above the fuel surface at atmospheric pressure, and most droplets were too small or too close to the fuel grain to be distinct from the main diffusion frame. Some droplets could be seen behind the fuel at atmospheric pressure; see Fig. 5. All pressurized tests looking at the combustion of paraffin showed intermittent, intense mass ejection events, which expelled bursts of droplets from the fuel surface. The intense mass ejection events expelled droplets in all directions away from the fuel surface, including upstream of the fuel grain. As the chamber pressure increased to supercritical pressures, it appeared that the time between these events decreased, the events became more violent, and the number of entrained droplets increased. The observed behavior at supercritical pressure was not a uniform heat transfer process from an evenly distributed flame with subsequent gentle melting of the fuel. Instead, the heat transfer appeared to be uneven, likely leading to nonuniform heat transfer, and potentially introducing mechanical stresses in the fuel grain surface thermal layer that further contributed to the mass transfer process. The uniformity of the flame was further investigated by looking at the top-down OH* chemiluminescence images; see Fig. 6. Here, the camera is looking down on the surface of a paraffin fuel grain at supercritical pressure. We can see that the flame appears to be nonuniform and even locally extinguished in some places.

The images in Fig. 4 contrast the appearance of the flame during nominal conditions and during an intense mass transfer event for four tests at low oxidizer mass fluxes. It was initially unclear whether the intense mass ejection behavior observed during these tests was an artifact of chuffing, an instability related to cooking of the fuel and subsequent thick melt layer formation and breakoff at low oxidizer mass fluxes [26]. Further tests sought to investigate this through a series of paraffin tests at higher oxidizer mass fluxes and a range of chamber pressures. The results for this test campaign are shown in Fig. 5, where it can be seen that the combustion mechanism, including the chamber pressure dependence observed in the original pressurized tests, remained unchanged by the increase in oxidizer mass flux.

It was possible that the changing nature of the droplet entrainment phenomena observed with varying combustion chamber pressure may have been due to the change in the dynamic pressure of the freestream flow rather than a fundamental change in the mass transfer mechanism at differing chamber pressures. Gater and L'Ecuyer argued that the surface roughness of the liquid layer decreases with increasing dynamic pressure of the gas flow [8]. To investigate this, we look at the roughness correction parameter Fr defined in Eq. (8). Equation (8) is the roughness parameter defined by Gater and Ecuyer [8] but rearranged and expressed in terms of motor parameters in Ref. [9]. We investigate the change in the surface roughness between tests 30 and 34, which were, respectively, conducted at atmospheric pressure and above the critical pressure of paraffin. There is some variability and uncertainty in the inputs to Eq. (8), which in turn produces a range of

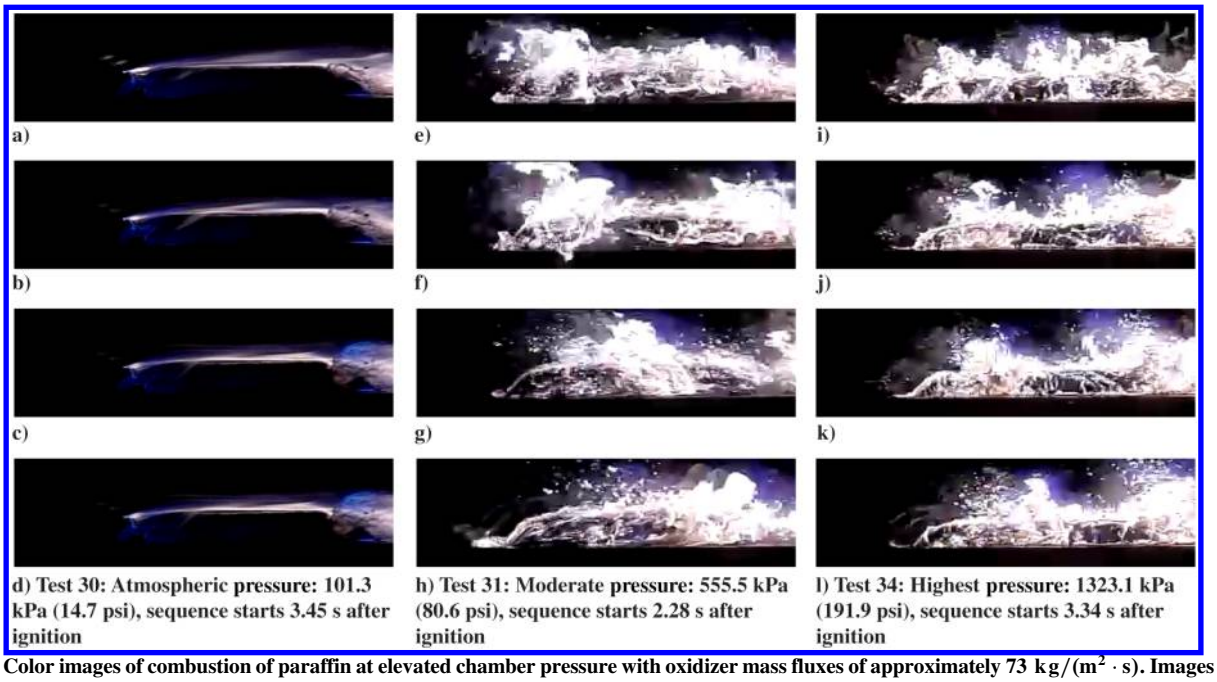

Fig. 5 Color images of combustion of paraffin at elevated chamber pressure with oxidizer mass fluxes of approximately 73 $\mathrm{kg/(m^2 \cdot s)}$. Images shown for each test are taken 1.67 ms apart. Oxidizer flow is from left to right. All images collected on camera 3, and camera settings are provided in the Appendix.

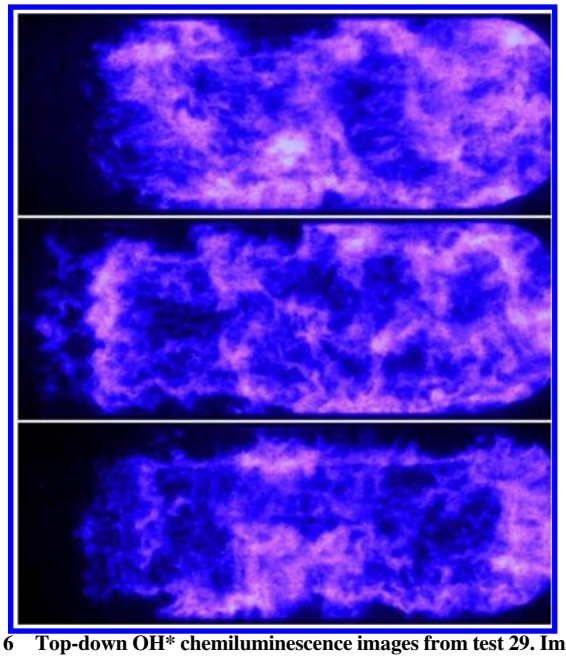

Fig. 6 Top-down OH* chemiluminescence images from test 29. Images shown for each test taken 16.7 ms apart, with first image (top) taken 0.66 s after ignition when chamber pressure was 1121.4 kPa (162.6 psi). Oxidizer flow is from left to right.

possible roughness correction values for each test. Accounting for this, the ratio of the roughness correction factor between these two tests is, at most, 1.6 [see Eq. (9)], which is not a significant enough change to account for the large change in the observed droplet entrainment mechanism for these two tests shown in Fig. 5:

$$Fr = 1 + \frac{14.1\rho_g^{0.4}}{G^{0.8}(T_g/T_v)^{0.2}} \tag{8}$$

$$\frac{Fr_{\mathrm{Test35}}}{Fr_{\mathrm{Test30}}} = 1.40\text{–}1.58 \tag{9}$$

Wax droplets must be removed from the quartz windows at the end of each pressurized test for the liquefying fuels. These droplets are deposited on the windows during the intense mass ejection events. They provide evidence that some liquid paraffin wax is transported beyond the main flame and into the freestream flow without combusting. Such behavior is to be expected from droplet combustion theory, even at supercritical pressures. Figure 7 shows schlieren images taken at the end of three blackened paraffin tests with consistent oxidizer mass fluxes. Wax deposits can be seen in each of the images. These images imply that, as the chamber pressure increases from atmospheric pressure, through subcritical pressures, to supercritical pressures, the size of the entrained droplets increases. As expected, no droplets are deposited on the windows for tests with classical fuels. Recall from Figs. 4 and 5 that it is extremely difficult to see droplets above the fuel surface in the atmospheric paraffin test images. However, Fig. 7 shows a large number of small unburned droplets deposited on the windows. Thus, what we see as droplets in the visuals may only constitute a relatively small fraction of the actual liquefied fuel mass coming off the surface.

IV. Quantitative Flame Location and Boundary-Layer Results

Image processing techniques were adopted to overlay and quantify the OH* chemiluminescence and schlieren image results. Image alignment was achieved using grid images recorded before each test. Edge detection techniques were applied to the schlieren images to identify the boundary-layer edge whereas peak OH* chemiluminescence intensities were used to locate the flame. Reference [25] provided the details of these processes. The overlaid images allowed the location of the flame within the boundary layer to be quantified. Figure 8 summarizes the results for the measured flame and boundary-layer location for the classical fuels of PMMA and high-density polyethylene (HDPE), as well as the liquefying fuel paraffin at atmospheric pressure. The results for each fuel grain shown are produced using 6001 consecutive images. Here, the top lines in each plot show the boundary-layer location, the middle lines show the flame location, and the bottom lines shown the fuel grain surface. The oxidizer mass flux for these tests ranges between 43.2 and 43.5 $\mathrm{kg/(m^2 \cdot s)}$, and the Re_{av} for each test ranges between 2.15×10^4 $\mathrm{cm^{-1}}$ and 2.16×10^4 $\mathrm{cm^{-1}}$. HDPE was included in this figure to demonstrate that this trend is consistent for the two representative classical fuels tested; it was not simply a feature of the combustion of PMMA. References [18,27] provided more details on the observed combustion behavior and properties of HDPE as a hybrid rocket fuel. Note that the location of the flame and boundary-layer edge depend upon the instantaneous fuel surface location. The instantaneous fuel surface location cannot be directly observed; instead, it was

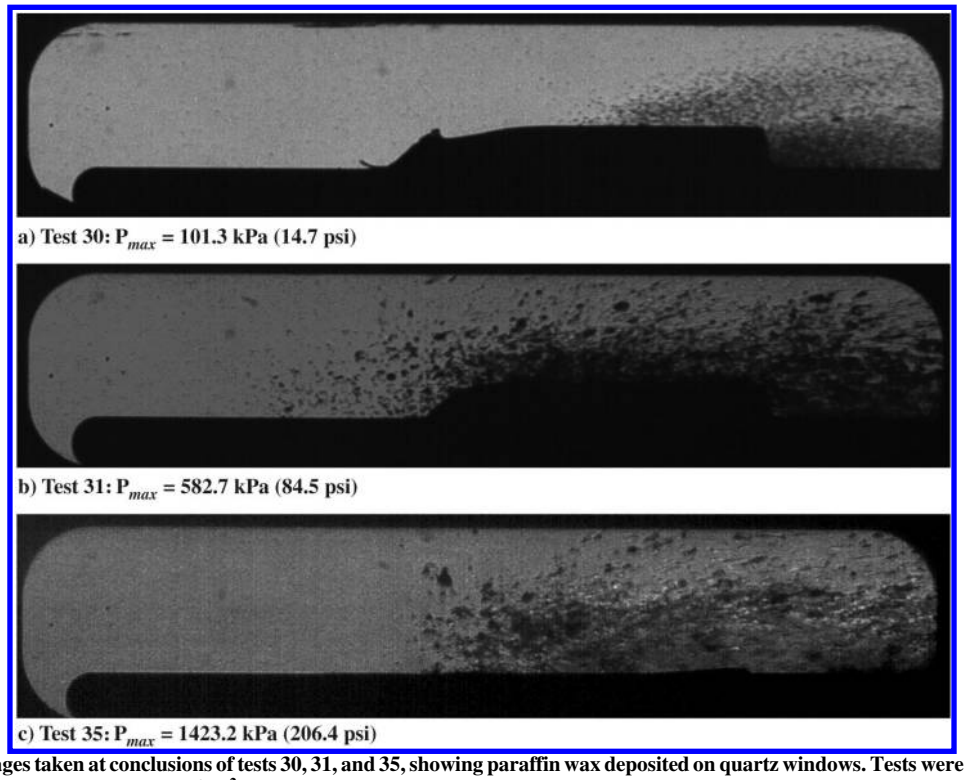

Fig. 7 Schlieren images taken at conclusions of tests 30, 31, and 35, showing paraffin wax deposited on quartz windows. Tests were all conducted with an oxidizer mass flux of approximately 73 $\mathrm{kg/(m^2 \cdot s)}$. Note that, at the end of test 35, all fuel has been consumed.

approximated using three different methods. Reference [25] provided the details of this estimation process. The thicker lines in Fig. 8 are due to greater uncertainty in the instantaneous fuel surface location; the thickness of the line corresponds to the range of expected values. The uncertainty in the fuel surface location constituted the largest source of error in the results, the flame location estimation error was within 0.1 mm, and the boundary-layer edge detection algorithm error was within 0.3 mm. See Ref. [18] for more detailed discussion of the error sources. Note also that, although the original paper also presented results for the classical fuels of Hydroxyl-Terminated PolyButadiene (HTPB) and Acrylonitrile Butadiene Styrene (ABS), they are not included here because these two fuels were structurally compromised, which likely affected their results. There were issues in the manufacture of these two fuel grains, leading to observed breakup of the fuels during combustion. Removing these two fuels from the results reveals an interesting trend; the flame location for the liquefying fuel is consistently farther from the fuel surface than the flame location for the classical fuels. Figure 8 also shows that, despite the difference in flame location, the boundary-layer height appears to be independent of the fuel at atmospheric pressure. Thus, the flame location as a function of boundary-layer height, which is a key assumption in hybrid combustion physics modeling, is observed to be greater for liquefying fuels than it is for classical fuels. To quantify the results of Fig. 8, we calculate the mean flame height within the boundary layer in the region between the vertical dotted lines to reduce the effects of artifacts from the leading and trailing edges of the fuel grain. We find that, at atmospheric pressure, the flame was located at approximately 33% of the boundary-layer height for classical fuels, and it was approximately 45% of the boundary-layer height for liquefying fuels.

The observation that the diffusion flame for liquefying fuels resides farther from the surface than that of classical fuels provides insight into the droplet entrainment mechanism. If the mass transfer rate is so much larger for paraffin, as we know it is, then it would be reasonable to expect that the flame might be farther from the fuel surface. However, this statement is not obvious when considering that much of the mass is contained in the droplets. One could easily argue that, because the fuel is mostly in the form of droplets, the main diffusion flame should be closer to the surface due to a reduced blocking effect. The results of Fig. 8 suggest that droplets coming off the fuel surface undergo a nonnegligible amount of evaporation before reaching the flame.

The results for the combustion of PMMA and blackened paraffin at an elevated chamber pressure also show a diffusion flame location for liquefying fuels farther from the surface than that of classical fuels; see Figs. 9 and 10, respectively. The boundary-layer edge is not shown for the highest-pressure tests for both PMMA and paraffin

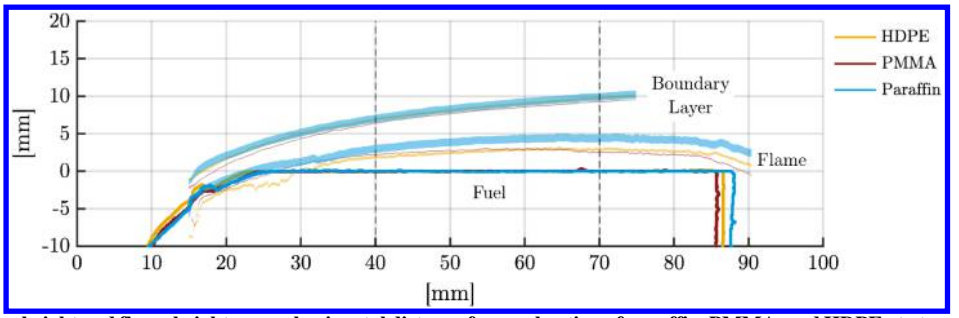

Fig. 8 Boundary-layer height and flame height versus horizontal distance for combustion of paraffin, PMMA, and HDPE at atmospheric pressure (tests 22, 21, and 19, respectively). Oxidizer flow is from left to right. The results for each fuel grain shown are produced using 6001 consecutive images.

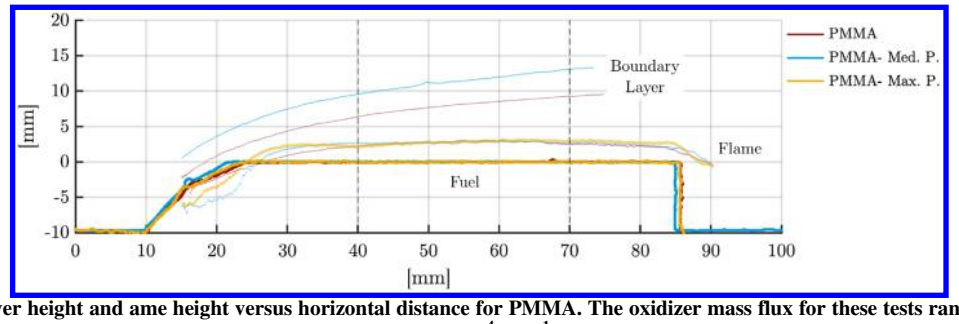

Fig. 9 Boundary layer height and ame height versus horizontal distance for PMMA. The oxidizer mass flux for these tests ranges between 43.2 and 43.5 kg/(m^2 · s). Test 21: $P_{av} = 101.3$kPa (14.7 psi), $Re_{av} = 2.16 \times 10^4$ cm^{-1}, and $N = 6001$ images. Test 16: $P_{av} = 433.3$ kPa (62.9 psi), $Re_{av} = 2.15 \times 10^4$ cm^{-1}, and $N = 814$ images. Test 23: $P_{av} = 930.2$ kPa (134.9 psi), $Re_{av} = 2.13 \times 10^4$ cm^{-1}, and $N = 1001$ images.

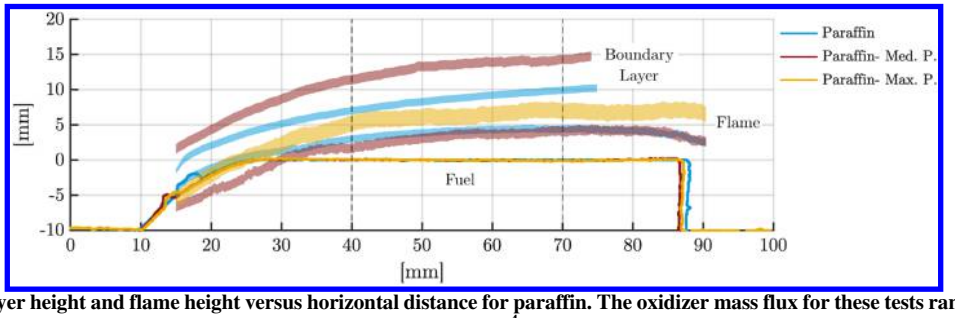

Fig. 10 Boundary layer height and flame height versus horizontal distance for paraffin. The oxidizer mass flux for these tests ranges between 43.3 and 43.5 kg/(m^2 · s). Test 22: $P_{av} = 101.3$ kPa (14.7 psi), $Re_{av} = 2.16 \times 10^4$, and $N = 6001$ images. Test 14: $P_{av} = 582.2$ kPa (84.4 psi), $Re_{av} = 2.16 \times 10^4$ cm^{-1}, and $N = 429$ images. Test 17: $P_{av} = 1236.9$ kPa (179.4 psi), $Re_{av} = 2.10 \times 10^4$ cm^{-1}, and $N = 1001$ images.

because, for these tests, it consistently moved beyond the edge of the observation window, precluding accurate measurement. Note again that the location of the flame and boundary-layer edge depend upon the instantaneous fuel surface location, which cannot be directly observed; thicker lines therefore represent greater uncertainty in this estimate. The region between the black vertical dashed lines, shown at horizontal locations of 40 and 70 mm, represents the region in which the flame location and the boundary-layer edge are evaluated.

It can be noted from the results of Fig. 9 that the diffusion flame location of PMMA is independent of chamber pressure, as would be expected from theory. The location of the flame for paraffin was the same for testing at atmospheric and moderate pressure, but it was farther from the fuel surface when the test pressure was above the critical pressure for paraffin wax. The boundary layer above both fuels is observed to thicken with increasing chamber pressure, which is likely due to the presence of instabilities at these elevated pressures. The thickening boundary layer serves to reduce the location of the flame as a percentage of boundary-layer height, with observed values in the range of 20%, which is around the upper bound of expected values from the theory of Marxman et al. [10].

The OH* and schlieren images were also used to explore the region within the boundary layer where combustion occurs. The hybrid combustion theory would predict this to be highly localized, with a typical approximation as a flame sheet for classical fuels. The nature of the droplet entrainment process would broaden the combustion region because combusting droplets can travel beyond the flame sheet toward the edge of the boundary layer. The thickness of the flame zone within the boundary layer was investigated by evaluating the vertical distribution of the flame at various points along the fuel grain. Figures 11 and 12 are provided to illustrate the relative flame zone thickness of fast-burning and classical hybrid rocket fuels, respectively. These figures show overlaid mean schlieren (shown in grayscale) and OH* chemiluminescence (shown in color) results. The PMMA results presented represent the analysis of the mean image of 6001 consecutive images. It was not possible to use this many consecutive images for paraffin because this would introduce error resulting from significant fuel regression. Instead, the paraffin results presented represent the analysis of the mean image of 101 consecutive images; during which, the fuel surface is expected to regress less than 0.02 mm. The flame thickness for all tests was quantified by calculating the mean OH* chemiluminescence image, normalizing the mean image to have unity peak brightness, and then looking at the variation in OH* intensity with height above the fuel grain at four different locations along the fuel grain. These four locations were selected around the center of the fuel grain to minimize unwanted artifacts near the leading and trailing edges of the fuel grain. The locations are shown in the top images in Figs. 11 and 12, and they correspond to x-axis locations of 40, 50, 60, and 70 mm in Figs. 8–10. The mean boundary-layer thickness and the flame location calculated using the original images and the method described previously are also shown in the four plots of OH* intensity for each figure.

A comparison of Figs. 11 and 12 implies that the flame zone for the high-regression-rate fuel is much larger than the classical fuel flame zone thickness. In fact, Fig. 11 shows combustion taking place right up to the edge of the boundary layer, whereas Fig. 12 consistently shows a region without combustion close to the edge of the boundary layer. This trend can also be seen in the individual images recorded at atmospheric pressure (Ref. [18]); it is not simply an artifact of taking the mean of many turbulent images.

Note that, for all fuels, the OH* chemiluminescence intensity at the fuel surface is not zero. This is to be expected because combustion is occurring along the sides of the fuel grain as well as on the top surface of the fuel. The OH* intensity at any height is a path-integrated value, and thus the positive contribution to the intensity from combustion along the sides of the grain would lead to a positive OH* intensity at the fuel surface in the image, even if there is no combustion on the surface of the fuel grain.

Evaluation of the flame zone thickness at elevated chamber pressures is challenging due to the highly unsteady and periodic nature of the flow during these tests. An accurate analysis requires a large number of images to be overlaid to generate a mean image, but this is not possible with the high fuel regression rates and the associated surface location errors. An attempt was made to look at representative individual images (see Ref. [18]), but these are not included here because a detailed analysis of single images can be highly variable and subject to greater error from slight differences in the record rate and/or triggering synchronization between the two high-speed cameras.

V. Combustion Instability Analysis

The pressurized combustion visualization tests all showed unsteady phenomena. All tests had steady upstream supply pressure and oxi-

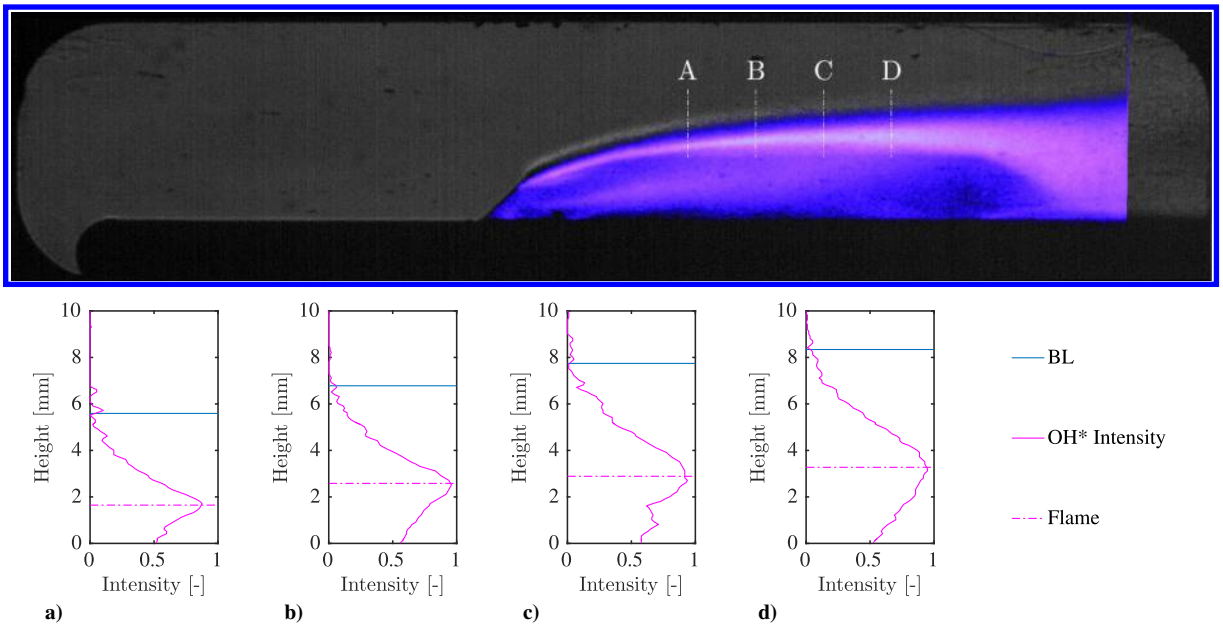

Fig. 11 Flame thickness of fast-burning fuel: paraffin. The figure is produced using 101 consecutive images, starting from image 10,000 of test 22. The normalized OH* intensity versus height above the fuel grain, the mean boundary-layer (BL) thickness, and the flame location calculated using the peak OH* intensity are provided at four different horizontal locations along the grain in Figs. 11a–11d.

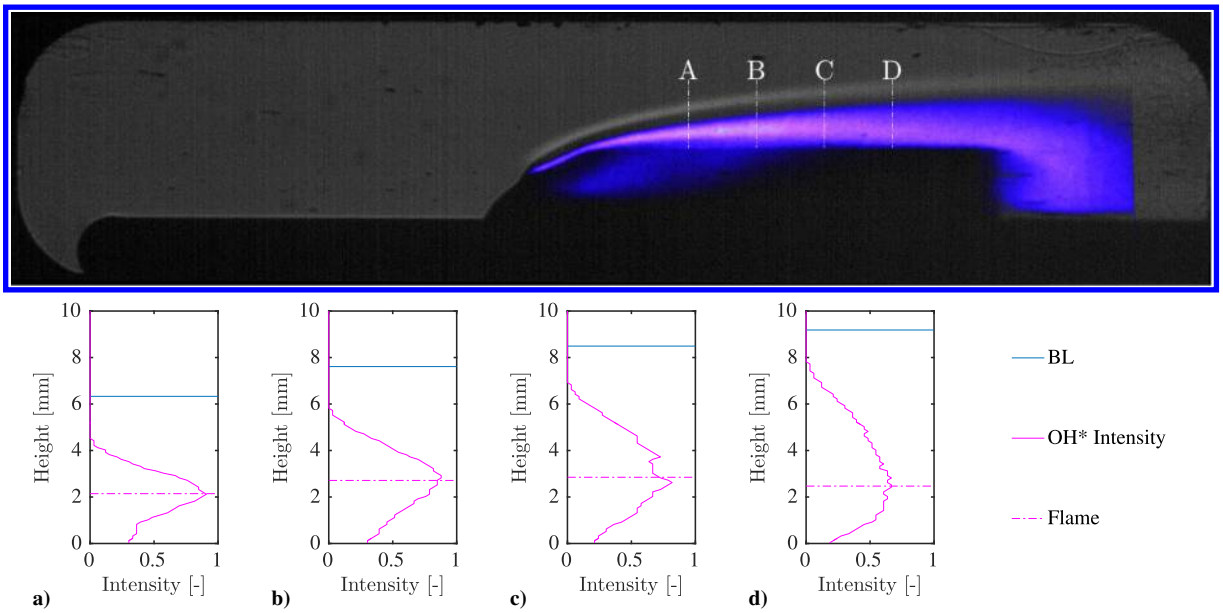

Fig. 12 Flame thickness of a classical fuel: PMMA. The figure is produced using 6001 consecutive images from test 21. The normalized OH* intensity versus height above the fuel grain, the mean boundary-layer thickness, and the flame location calculated using the peak OH* intensity are provided at four different horizontal locations along the grain in Figs. 12a–12d.

dizer mass flow rate; however, there appears to be a number of other sources of unsteadiness in the schlieren, OH* chemiluminescence, and visual high -peed videos. The most notable of these is a large-scale unsteadiness in mass ejection for paraffin fuels. This section seeks to characterize the possible sources of this unsteadiness using a spectral analysis of the images and combustion chamber pressure.

Spectral results for the combustion of paraffin at combustion chamber pressures above the critical pressure of the fuel (namely, for test 17 and test 29) are provided in Figs. 13 and 14. The only difference in operating conditions between these two tests is a slightly increased mass flux resulting from the use of a window in the upper wall of the test section, with two brass blanks replacing the side windows to enable the OH* top view for test 29. The normalized spectral content (fast Fourier transform) presented in Figs. 13c–13f is calculated using the data between the vertical dashed lines in Figs. 13a and 13b. The spectral content of the chamber pressure for test 17 is calculated after detrending the data with a cubic fit and has a resolution of 0.4 Hz. The spectral content of the chamber pressure for test 29 is calculated after detrending the data with a linear fit and has a resolution of 0.7 Hz. The spectral content of the combustion chamber pressure for these tests (Figs. 13c and 13d) indicates a combustion instability of around 200 Hz. An analysis of cold flow data for the system provides evidence that this 200 Hz oscillation is well below the acoustic modes of the chamber. The pressure drop across the orifice in the oxidizer feed line is sufficient to ensure choked flow throughout each test. The oxidizer mass flow rate data for these tests also do not show any notable oscillation, and thus the 200 Hz mode is not the result of a feed-couple instability. The temporal variation in mean OH* intensity for each image (see Figs. 13c and 13f) provides almost no useful spectral information to explore the instability.

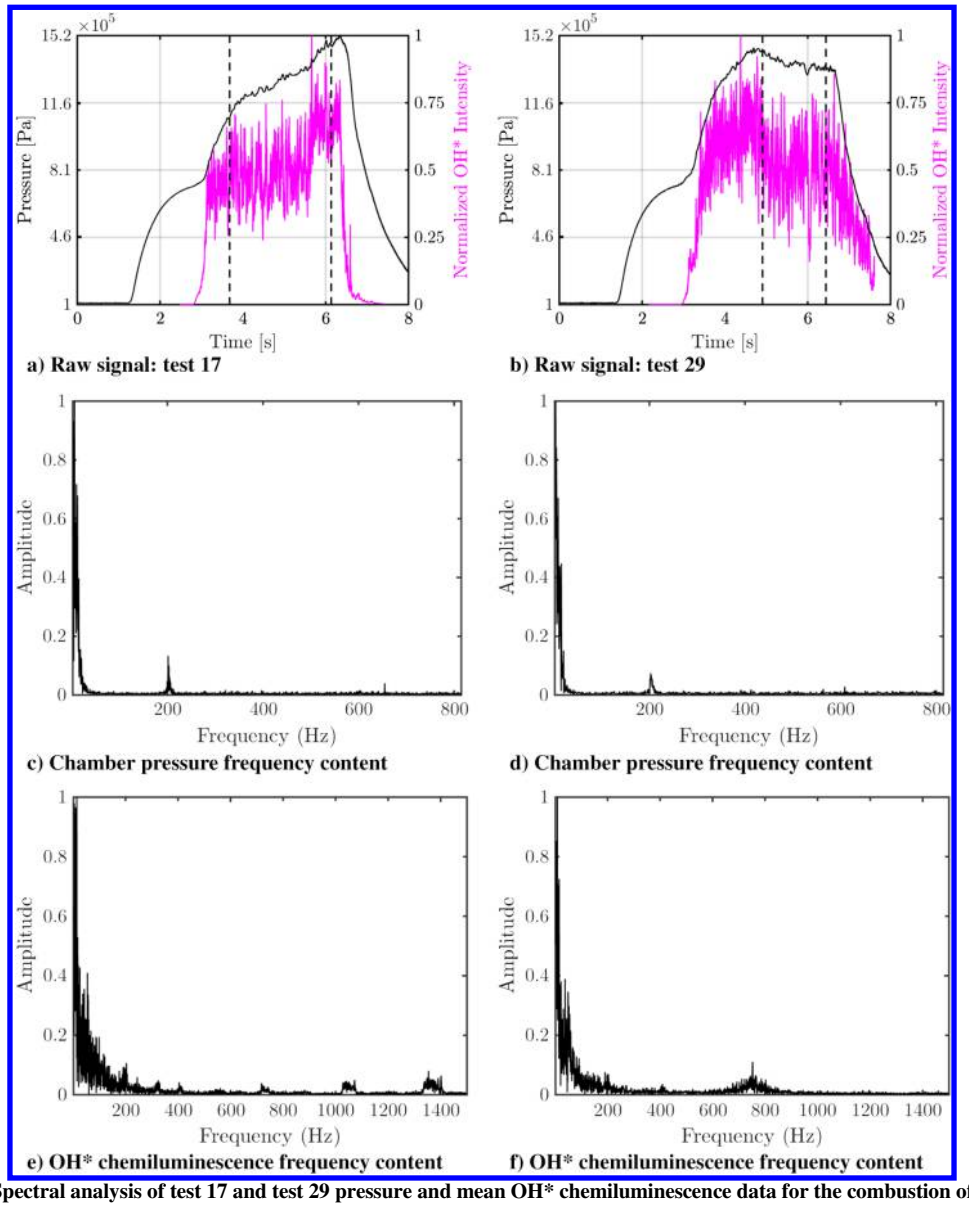

Fig. 13 Spectral analysis of test 17 and test 29 pressure and mean OH* chemiluminescence data for the combustion of paraffin.

Instead, the OH* intensity spectral content must be evaluated separately for each pixel. This approach was adopted to produce Fig. 14, where the 200 Hz instability can be clearly seen around the leading edge of the fuel grain. Figures 14a and 14b show the amplitude of the OH* chemiluminescence signal in the Fourier domain for each pixel at the peak frequency for that test. This peak frequency is defined as the frequency with the greatest single pixel amplitude. The location of the pixel at which this peak amplitude occurs is indicated in the figure. Figures 14c and 14d show the complete frequency content of the OH* chemiluminescence signal for the peak pixel. Observation of color and OH* chemiluminescence images for test 17 and test 29 show highly unsteady behavior down the length of the fuel grain. However, the results of Fig. 14 indicate that the source of this unsteadiness is localized at approximately 200 Hz around the leading edge of the fuel grain. The top view of the fuel grain (Fig. 14b) indicates that this oscillation is symmetric across the surface of the fuel.

The observed unsteadiness in the flame is attributed to two sources. The paraffin tests appear to have inherent unsteadiness associated with the mass transfer mechanism of this high-regression-rate fuel. All tests also appear to be subject to a flameholding instability associated with the leading edge of the fuel grain. The leading edge of the fuel grain is akin to a forward-facing step with uniform freestream flow ahead of the grain. This forward-facing step acts to destabilize the flow. A typical hybrid rocket motor injects the oxidizer into the combustion chamber. There is usually a large area ratio between the combustion chamber and the injector, which effectively acts like a rearward-facing step, creating recirculating regions that act to stabilize the flow and anchor the flame to the head end of the motor.

Flameholding instabilities are not typically discussed in the context of hybrid rocket motors. The presence of this instability in nearly all of the visualization experiment tests, observed as the continued cyclic motion of the flame at the leading edge of the fuel grain, can be attributed to the nontraditional combustion chamber geometry. Story (Ref. [28]) highlighted the need to anchor a flame at the head end of a hybrid motor to ensure combustion stability. Flameholding instabilities, also referred to as chugging, are commonly discussed in liquid rocket engine literature. The description of this instability as applied to liquid rocket engines provided by Huzel and Huang [29] can be read as a blow-by-blow description of the processes observed in the hybrid rocket visualization experiment described here. They associate chugging with an accumulation of fuel followed by subsequent higher-rate combustion. "The resulting chamber pressure spikes cause a reduction, or even reversal, of the propellant flows and a consequent rapid collapse of chamber pressure, allowing propellants to rush in and repeat the cycle" [29]. The schlieren images of the freestream recorded for the pressurized visualization tests show such reversal in the oxidizer flow interspersed with explosive combustion events, which is consistent with this description.

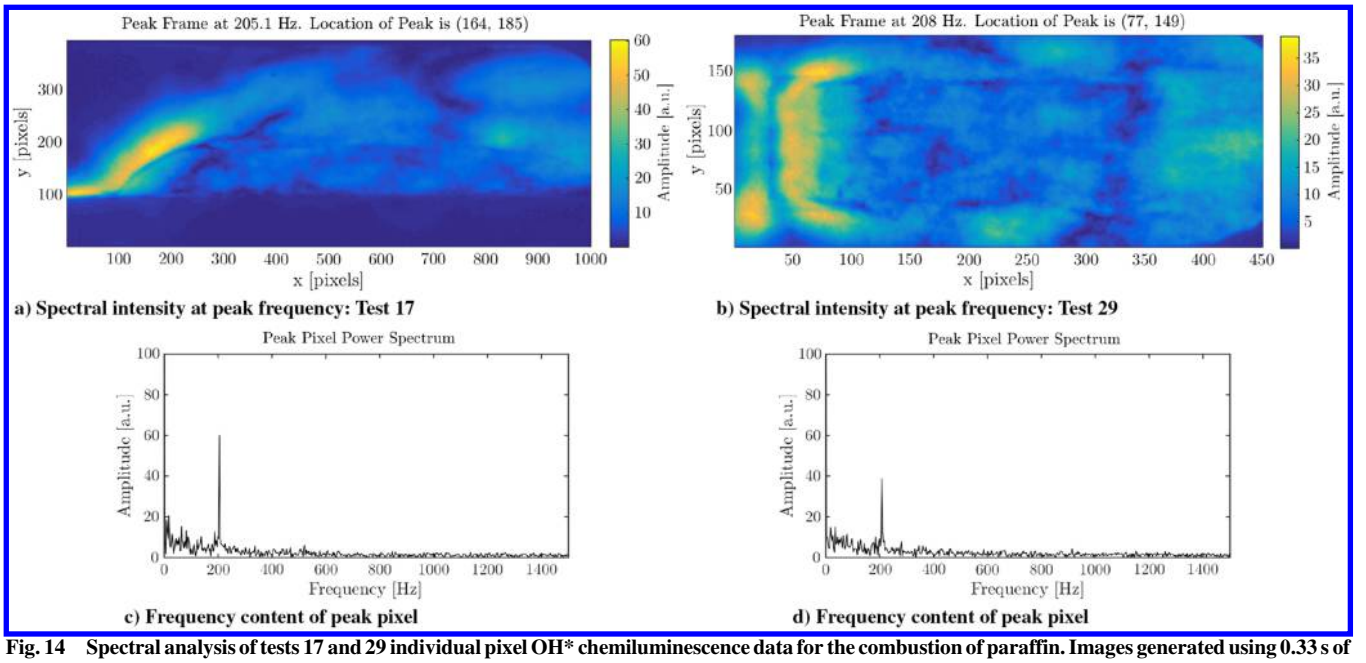

Fig. 14 Spectral analysis of tests 17 and 29 individual pixel OH* chemiluminescence data for the combustion of paraffin. Images generated using 0.33 s of OH* chemiluminescence data starting from left vertical dashed lines in Figs. 13a and 13b.

VI. Conclusions

The combustion of a high-regression-rate liquefying fuel and gaseous oxygen was successfully recorded on schlieren, OH* chemiluminescence, and color high-speed video at a range of chamber pressures. The nature of the combustion was seen to change dramatically with increasing pressure, up to approximately the critical pressure of the fuel. The droplet entrainment mechanism proposed by Karabeyoglu et al. [2] was observed at all pressures.

The location of the flame within the boundary layer was quantified for a range of fuels at atmospheric pressure. The thickness of the boundary layer above the fuel grain at atmospheric pressure appeared to be unaffected by the selection of fuel. The flame location, however, was observed to sit closer to the fuel surface for the classical fuels, and it was farther from the fuel surface for the high-regression-rate fuel. At atmospheric pressure, the detected flame locations are consistently greater than the original values of 10–20% predicted from theory by Marxman et al. [10], but they are within the range of values around 50% observed by Wooldridge and Muzzy [21]. At atmospheric pressure, the flame zone for the fast-burning fuel (paraffin) was seen to be much thicker than the flame zone of the classical fuels, extending almost to the edge of the boundary layer. This observation is consistent with the droplet entrainment mechanism.

The location of the flame within the boundary layer was also quantified at elevated chamber pressures. The height of the flame above the fuel surface was unaffected by the increase in chamber pressure, or the presence of a combustion instability, for the classical fuel. It also remained constant for the liquefying fuel for the two tests conducted at low pressure, but it moved farther from the fuel surface for the test above the critical pressure of the fuel. The increase in chamber pressure consistently corresponded to an increase in height of the boundary layer above the fuel grain for all tests conducted, which was likely due to the presence of a flameholding combustion instability. The flame height as a percentage of the boundary-layer thickness was therefore observed to decrease with increasing chamber pressure, approaching or achieving a value of 20%, near the upper range of the theoretical prediction by Marxman et al. [10]. However, the apparent flame height variability with pressure is not contained in the current hybrid rocket combustion theory and may be due to the presence of the combustion instability.

The results of the combustion visualization experiment confirmed the basic droplet entrainment mechanism for high-regression-rate fuels proposed by Karabeyoglu et al. [2] at a range of combustion chamber pressures, including supercritical pressures. Entrained filament structures were not observed to be the dominant feature at chamber pressures above the critical pressure of the fuel; instead, at high pressures, numerous intense mass ejection events emitting large numbers of droplets were observed to be a major mass transfer mechanism. The nature of the combustion for these high-regression-rate fuels burning at elevated chamber pressures was generally observed to be more intermittent, with the main diffusion flame appearing to be locally extinguished in places. A schematic of the observed nature of the combustion of high-regression-rate fuels is shown schematically alongside the original proposed droplet entrainment mechanism; see Fig. 15.

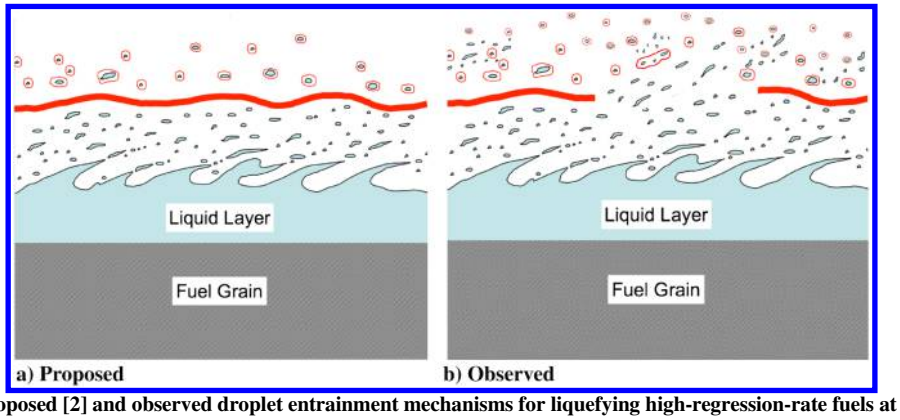

Fig. 15 Schematic of proposed [2] and observed droplet entrainment mechanisms for liquefying high-regression-rate fuels at supercritical pressures.

Appendix: Test Details and Summary of Other Visualization Experiments

Table A1 Summary table of main parameters for each test

Test no.	Date	Fuel[a]	Maximum P_c, kPa (psi)	G_{Ox}, kg/(m^2 · s)	t_b, [b]s	Δm_f, [c]g
7	30 June 2014	Paraffin	294.9 (42.8)	20.5	3.5	2.3
8	30 June 2014	Paraffin	490.0 (71.1)	36.6	3.5	5.1
9	1 July 2014	Paraffin	835.8 (121.2)	20.4	3.5	6.7
10	4 July 2014	Paraffin	1175.0 (170.4)	36.3	3.5	8.2
14	18 July 2014	Paraffin	616.8 (89.5)	43.4	3.5	6.7
16	23 July 2014	PMMA	444.0 (64.4)	43.3	3.5	2.1
17	25 July 2014	Paraffin	1524.2 (221.1)	43.3	3.5	17.5
19	4 August 2014	HDPE	101.3 (14.7)	43.2	3.5	0.9
21	5 August 2014	PMMA	101.3 (14.7)	43.2	5	2.0
22	6 August 2014	Paraffin	101.3 (14.7)	43.5	3.5	4.1
23	6 August 2014	PMMA	948.3 (137.5)	43.3	3.5	4.0
29	8 August 2014	Paraffin-top	1455.7 (211.1)	54.3	3.5	12.9
30	2 June 2015	Paraffin	101.3 (14.7)	74.4	4	6.1
31	3 June 2015	Paraffin	582.7 (84.5)	73.1	3.5	8.5
34	8 June 2015	Paraffin	1430.3 (207.4)	73.1	3.5	13.5
35	9 June 2015	Paraffin	1423.2 (206.4)	73.0	3.5	13.4

[a]The suffix "Top" after a fuel name refers to the fact that this test was conducted with the diving board rotated 90 deg, allowing OH* images of the top of the fuel grain. Schlieren images could not be recorded for these tests. Tests 28 and 29 in this configuration had two brass blanks and one window installed, leading to an increase in the oxidizer mass flux for these tests relative to the other 2014 tests.
[b]The burn time listed here is the preprogrammed burn time without the ignition or purge onset delays accounted for.
[c]The burnt mass listed in this table is calculated by weighing the fuel grains before and after each test. All fuel left on the diving board at the end of a test is considered unburned. The mass of fuel burned is significantly higher for test 22 as the fuel grain lifted off the diving board during this test.

Table A2 Color camera settings for visualization experiment hot fires discussed in this paper (FPS, frames per second; Fstop, f-stop; SS, shutter speed; ISO, image sensor; 1/, 1/20,000)

	Camera 2 settings				Camera 3 settings			
Test	FPS, /s	Fstop	SS, 1/	ISO	FPS, /s	Fstop	SS, 1/	ISO
7	1200	2.7	20,000	400	1200	2.7	20,000	200
8	1200	2.7	20,000	400	1200	2.7	20,000	200
9	1200	2.7	20,000	400	1200	2.7	20,000	200
10	1200	2.7	32,000	400	1200	2.7	32,000	200
14	Camera malfunctioned				Camera malfunctioned			
16	1200	2.7	32,000	200	1200	2.7	32,000	200
17	1200	3	40,000	100	Camera malfunctioned			
19	1200	2.7	32,000	100	1200	2.7	32,000	100
21	1200	2.7	20,000	200	1200	2.7	20,000	200
22	Camera malfunctioned				Camera malfunctioned			
23	Camera malfunctioned				Camera malfunctioned			
29	1200	2.7	40,000	100	Camera malfunctioned			
30	1200	2.7	16,000	200	1200	2.7	16,000	100
31	1200	2.7	40,000	100	1200	2.7	40,000	100
34	1200	3.3	40,000	100	1200	3.8	40,000	100
35	1200	3.8	40,000	100	Camera malfunctioned			

Table A3 Schlieren camera settings for visualization experiment hot fires discussed in this paper[a]

Test	Frame rate, /s	Exposure, μs	Gain	Image size [–] × [–]	Frames	Lens size, mm
7	3000	100	2	1080 × 236	14,207	105
8	3000	200	2	1080 × 236	14,207	105
9	3000	95	2	1080 × 236	14,207	105
10	3000	45	2	1080 × 236	14,207	105
14	3000	13	2	1080 × 236	14,207	105
16	3000	13	2	1080 × 236	14,207	105
17	3000	13	2	1080 × 236	14,207	105
19	3000	13	2	1080 × 236	14,207	105
21	3000	13	2	1080 × 236	14,207	105
22	3000	13	2	1080 × 236	14,207	105
23	3000	13	2	1080 × 236	14,207	105
29	Top view: schlieren not used					
30	3000	15	2	1080 × 236	14,207	105
31	3000	13	2	1080 × 236	14,207	105
34	Camera triggered too early					
35	3000	18	2	1080 × 236	14,207	105

[a]Schlieren images are recorded at 3000 fps using Motion Studio software. The lens used had an f number of $f/2.8$

Table A4 OH* chemiluminescence camera settings for visualization experiment hot fires discussed in this paper

Test	FPS, /s	Exposure, μs	ROI	Frames	Gain, V	Aperture, $f/\#$
14	3000	4	512×256	16,385	3.8	$f/8$
16	3000	4	512×256	16,385	3.8	$f/8$
17	3000	2	512×256	16,385	3.8	$f/8$
19	3000	7	512×256	16,385	3.8	$f/8$
21	3000	11	512×256	16,385	3.8	$f/8$
22	3000	12	512×256	16,385	3.8	$f/8$
23	3000	3	512×256	16,385	3.8	$f/8$
29	3000	2.5	512×256	16,385	3.8	$f/8$

Table A5 Summary of other hybrid rocket visualization experiments

	Author(s)	Experiment	Propellants	Imaging/ results	Pressure	Oxidizer mass flux	Year	Reference
United technology center (UTC)	Marxman, Muzzy and Wooldridge	Slab burner with a wind tunnel upstream	PMMA/gaseous oxygen (GOx)	Shadowgraph and schlieren	Atmospheric	Low	1963	[10]
Jet Propulsion Laboratory	Strand et al.	Slab burner (either single or two opposing fuel slabs) with two windows (leading and trailing edges)	HTPB fuel grains embedded with coal and aluminum particles	No combustion images were ever published.	$\geq$ 1379 kPa (200 psi)	$\leq$ 35 kg/(m^2 · s)	1992	[30]
Pennsylvania State University	Chiavrini et al.	Slab burner (two opposing) with graphite windows	HTPB (and HTPB plus 20% aluminum (Al)) and GOx	X-ray radiography, ultrasonic pulse echo	1.17–5.52 MPa [170–800 psia]	105–457 kg/(m^2 · s)	1990s–2000s	[31, 32,12]
	Evans et al.	X-ray translucent hybrid casing motor	Paraffin (and metalized paraffin) with GOx	X-ray radiography	2.17–4.24 MPa [300–600 psia]	163–320 kg/(m^2 · s)	2009	[33]
NASA Ames Research Center	Zilliac [18]	Large-scale motor	— —	Failed due to issues sealing. No images of entrainment were obtained.	Elevated pressure	— —	2003	— —
ONERA	Pelletier	Hybrid combustion Analysis for regression rate evaluation (HYCARRE). Flows hot gas over hybrid fuels, observing the fuel surface through two optical windows. No combustion of fuels.	— —	Particle image velocimetry (PIV) of the hot-gas flow and ultrasonic sensors for instantaneous fuel grain measurements	— —	— —	2009	[34]
Tokai University	Nakagawa et al., Nakagawa and Nikone, and Hikone et al.	Slab burner and cylindrical motor with optical access to the postcombustion chamber	Wax (C51H104) with GOx	Optical	Atmospheric pressure	10–30 kg/(m^2 · s)	2009 and 2011	[35–37]
Polytechnic University of Milan	DeLuca et al.	Two-dimensional radial microburner with a single optical port	HTPB and paraffin with GOx	Used dark regions of color images as the approximate instantaneous location of the fuel grain	— —	— —	2011	[38]
Akita University	Wada et al.	Slab burner (opposing slabs of fuel)	PMMA and a low-melting-point thermoplastic fuel with GOx	The number and size of the entrained droplets are independent of chamber pressure.	Up to 2 MPa (290 psi)	<= 35 kg/(m^2 · s)	2013	[15]
Purdue University	Shark et al.	Strand suspended in a cylindrical and acrylic combustion chamber	HTPB and dicyclopentadiene with GOx	Optical	Elevated pressure	200 kg/(m^2 · s)	2013	[39]
DLR, German Aerospace Center	Petrarolo et al., Kobald et al., and Petrarolo et al.	Slab burner	Paraffin and GOx	High-speed visual and schlieren images report visualization of droplet entrainment	Atmospheric pressure, elevated pressure	<= 10.93 kg/(m^2 · s)	2013, 2015, 2017, 2018	[16, 40–43]

Acknowledgments

The authors would like to thank the Jet Propulsion Laboratory's Strategic University Research Partnership program and the Stanford Center of Excellence in Aeronautics and Astronautics for financial support of this project. E. Jens also acknowledges the support of Zonta International in the form of the Amelia Earhart Fellowship. The authors thank Greg Zilliac, Rabi Mehta, and James Heineck of NASA Ames Research Center for loaning the MotionPro X3 Plus for this work, as well as Campbell Carter of the U.S. Air Force Research Laboratory for loaning the Photron APX i^2. For E. T. Jens and A. C. Karp, this work was done as a private venture and not in the authors' capacities as employees of the Jet Propulsion Laboratory, California Institute of Technology.

References

[1] Cantwell, B. J., Karabeyoglu, M. A., and Altman, D., "Recent Advances in Hybrid Propulsion," *International Journal of Energetic Materials and Chemical Propulsion*, Vol. 9, No. 4, 2010, pp. 305–326. https://doi.org/10.1615/IntJEnergeticMaterialsChemProp.v9.i4

[2] Karabeyoglu, M. A., Cantwell, B. J., and Altman, D., "Development and Testing of Paraffin-Based Hybrid Rocket Fuels," AIAA Paper 2001-4503, 2001. https://doi.org/10.2514/6.2001-4503

[3] Chandler, A. A., Cantwell, B. J., Hubbard, G. S., and Karabeyoglu, M. A., "A Two-Stage, Single Port Hybrid Propulsion System for a Mars Ascent Vehicle," AIAA Paper 2010-6635, 2010. https://doi.org/10.2514/6.2010-6635

[4] Chandler, A. A., Cantwell, B. J., and Hubbard, G. S., "Hybrid Propulsion for Solar System Exploration," AIAA Paper 2011-6103, 2011. https://doi.org/10.2514/6.2011-6103

[5] Jens, E., Cantwell, B. J., and Hubbard, G. S., "Hybrid Rocket Propulsion Systems for Outer Planet Exploration Missions," *Acta Astronautica*, Vol. 128, Nov.–Dec. 2016, pp. 119–130. https://doi.org/10.1016/j.actaastro.2016.06.036

[6] Karp, A. C., Nakazono, B., Benito Manrique, J., Shotwell, R., Vaughan, D., and Story, G. T., "A Hybrid Mars Ascent Vehicle Concept for Low Temperature Storage and Operation," AIAA Paper 2016-4962, 2016. https://doi.org/10.2514/6.2016-4962

[7] Shotwell, R., Benito, J., Karp, A., and Dankanich, J., "Drivers, Developments and Options Under Consideration for a Mars Ascent Vehicle," *2016 IEEE Aerospace Conference*, IEEE Publ., Piscataway, NJ, 2016, Paper 114. https://doi.org/10.1109/AERO.2016.7500822

[8] Gater, R. A., and L'Ecuyer, M. R., "A Fundamental Investigation of the Phenomena that Characterize Liquid-Film Cooling," *International Journal of Heat and Mass Transfer*, Vol. 13, No. 12, 1970, pp. 1925–1939. https://doi.org/10.1016/0017-9310(70)90093-19310(70)90093–1

[9] Karabeyoglu, M. A., Altman, D., and Cantwell, B. J., "Combustion of Liquefying Hybrid Propellants: Part 1, General Theory," *Journal of Propulsion and Power*, Vol. 18, No. 3, 2002, pp. 610–620. https://doi.org/10.2514/2.5975

[10] Marxman, G. A., Muzzy, R., and Wooldridge, C., "Fundamentals of Hybrid Boundary Layer Combustion," *Heterogeneous Combustion Conference*, AIAA Paper 1963-0505, 1963. https://doi.org/10.2514/6.1963-505

[11] Marxman, G. A., "Combustion in the Turbulent Boundary Layer on a Vaporizing Surface," *Symposium (International) on Combustion*, Vol. 10, No. 1, 1965, pp. 1337–1349. https://doi.org/10.1016/S0082-0784(65)80268-5

[12] Chiaverini, M., "Review of Solid-Fuel Regression Rate Behavior in Classical and Nonclassical Hybrid Rocket Motors," *Fundamentals of Hybrid Rocket Combustion and Propulsion*, Vol. 218, Progress in Astronautics and Aeronautics, edited by M. J. Chiaverini, and K. K. Kuo, AIAA, Reston, VA, 2007, pp. 37–126. https://doi.org/10.2514/5.9781600866876.0037.0126

[13] Karabeyoglu, M. A., Cantwell, B. J., and Stevens, J., "Evaluation of the Homologous Series of Normal Alkanes as Hybrid Rocket Fuels," AIAA Paper 2005-3908, 2005. https://doi.org/10.2514/6.2005-3908

[14] Haapanen, S. I., "Linear Stability Analysis and Direct Numerical Simulation of a Miscible Two-Fluid Channel Flow," Ph.D. Thesis, Stanford Univ., Stanford, CA, 2008.

[15] Wada, Y., Kato, R., Kato, N., and Hori, K., "Observation of the Surface Regression Behavior of Hybrid Rocket Fuel Using a Slab Motor," *64th International Astronautical Congress*, International Astronautical Federation, Beijing, PRC, 2013, pp. 5–9.

[16] Petrarolo, A., Kobald, M., and Schlechtriem, S., "Visualization of Combustion Phenomena in Paraffin-Based Hybrid Rocket Fuels at Super-Critical Pressures," AIAA Paper 2018-4927, 2018. https://doi.org/10.2514/6.2018-4927

[17] Chandler, A. A., "An Investigation of Liquefying Hybrid Rocket Fuels with Applications to Solar System Exploration," Ph.D. Thesis, Stanford Univ., Stanford, CA, 2012.

[18] Jens, E. T., "Hybrid Rocket Combustion and Applications to Space Exploration Missions," Ph.D. Thesis, Stanford Univ., Stanford, CA, 2015.

[19] Gordon, S., and McBride, B. J., "Computer Program for Calculation of Complex Chemical Equilibrium Compositions and Applications," Vol. 19, NASA, Office of Management, Scientific and Technical Information Program Rept. NASA-RP-1311, 1996.

[20] Corrsin, S., and Kistler, A. L., "Free-Stream Boundaries of Turbulent Flows," NACA TR-1244, Jan. 1955.

[21] Wooldridge, C., and Muzzy, R., "Measurements in a Turbulent Boundary Layer with Porous Wall Injection and Combustion," *Symposium (International) on Combustion*, Vol. 10, No. 1, 1965, pp. 1351–1362. https://doi.org/10.1016/S0082-0784(65)80269-7

[22] Muzzy, R., and Wooldridge, C., "Boundary-Layer Turbulence Measurements with Mass Addition and Combustion," *AIAA Journal*, Vol. 4, No. 11, 1966, pp. 2009–2016. https://doi.org/10.2514/3.3832

[23] Soid, S., and Zainal, Z., "Spray and Combustion Characterization for Internal Combustion Engines Using Optical Measuring Techniques A Review," *Energy*, Vol. 36, No. 2, 2011, pp. 724–741. https://doi.org/10.1016/j.energy.2010.11.022

[24] Guethe, F., Guyot, D., Singla, G., Noiray, N., and Schuermans, B., "Chemiluminescence as Diagnostic Tool in the Development of Gas Turbines," *Applied Physics B*, Vol. 107, No. 3, 2012, pp. 619–636. https://doi.org/10.1007/s00340-012-4984-y

[25] Jens, E. T., Miller, V. A., and Cantwell, B. J., "Schlieren and OH* Chemiluminescence Imaging of Combustion in a Turbulent Boundary Layer over a Solid Fuel," *Experiments in Fluids*, Vol. 57, No. 3, 2016, pp. 1–16. https://doi.org/10.1007/s00348-016-2124-x

[26] Karabeyoglu, A, "Combustion Instability and Transient Behavior in Hybrid Rocket Motors," *Fundamentals of Hybrid Rocket Combustion and Propulsion*, Vol. 218, Progress in Astronautics and Aeronautics, edited by M. J. Chiaverini, and K. K. Kuo, AIAA, Reston, VA, 2007, pp. 351–412. https://doi.org/10.2514/5.9781600866876.0351.0412

[27] Chandler, A. A., Jens, E. T., Cantwell, B. J., and Hubbard, G. S., "Visualization of the Liquid Layer Combustion of Paraffin Fuel at Elevated Pressures," *63rd International Astronautical Congress*, International Astronautical Federation (IAF), Paris, France, 2012.

[28] Story, G, "Large-Scale Hybrid Motor Testing, American Institute of Aeronautics and Astronautics," *Fundamentals of Hybrid Rocket Combustion and Propulsion*, Vol. 218, Progress in Astronautics and Aeronautics, edited by M. J. Chiaverini, and K. K. Kuo, AIAA, Reston, VA, 2007, pp. 513–552. https://doi.org/10.2514/5.9781600866876.0513.0552

[29] Huzel, D. K., and Huang, D. H., *Modern Engineering for Design of Liquid-Propellant Rocket Engines*, Vol. 147, AIAA, Washington, D.C., 1992, p. 130. https://doi.org/10.2514/4.866197

[30] Strand, L., Ray, R., Anderson, F., and Cohen, N., "Hybrid Rocket Fuel Combustion and Regression Rate Study," AIAA Paper 1992-3302, 1992. https://doi.org/10.2514/6.1992-3302

[31] Chiaverini, M. J., Serin, N., Johnson, D. K., Lu, Y.-C., Kuo, K. K., and Risha, G. A., "Regression Rate Behavior of Hybrid Rocket Solid Fuels," *Journal of Propulsion and Power*, Vol. 16, No. 1, 2000, pp. 125–132. https://doi.org/10.2514/2.5541

[32] Chiaverini, M. J., Kuo, K. K., Peretz, A., and Harting, G. C., "Regression-Rate and Heat Transfer Correlations for Hybrid Rocket Combustion," *Journal of Propulsion and Power*, Vol. 17, No. 1, 2001, pp. 99–110. https://doi.org/10.2514/2.5714

[33] Evans, B., Boyer, E., Kuo, K., Risha, G., and Chiaverini, M., "Hybrid Rocket Investigations at Penn State University's High Pressure Combustion Laboratory: Overview and Recent Results," AIAA Paper 2009-5349, 2009. https://doi.org/10.2514/6.2009-5349

[34] Pelletier, N., "Etude des Phenomenes de Combustion dans un Propulseur Hybride Modelisation et Analyse Experimentale de la Regression des Combustibles Liquefiables," Ph.D. Thesis, Univ. of Toulouse, Toulouse, France, 2009.

[35] Nakagawa, I., Hikone, S., and Suzuki, T., "Study on the Regression Rate of Paraffin-Based Hybrid Rocket Fuels," AIAA Paper 2009-4935, 2009. https://doi.org/10.2514/6.2009-4935

[36] Nakagawa, I., and Nikone, S., "Study on the Regression Rate of Paraffin-Based Hybrid Rocket Fuels," *Journal of Propulsion and Power*, Vol. 27, No. 6, 2011, pp. 1276–1279. https://doi.org/10.2514/1.B34206

[37] Hikone, S., Maruyama, S., Isiguro, T., and Nakagawa, I., "Regression Rate Characteristics and Burning Mechanism of Some Hybrid Rocket Fuels," AIAA Paper 2010-7030, 2010. https://doi.org/10.2514/6.2010-7030

[38] DeLuca, L., Galfetti, L., Maggi, F., Colombo, G., Paravan, C., Reina, A., Tadini, P., Sossi, A., and Duranti, E., "An Optical Time-Resolved Technique of Solid Fuels Burning for Hybrid Rocket Propulsion," AIAA Paper 2011-5753, 2011. https://doi.org/10.2514/6.2011-5753

[39] Shark, S. C., Zaseck, C. R., Pourpoint, T. L., Son, S. F., and Heister, S. D., "Visualization and Performance of Hybrid Rocket Solid Fuels in an Optical Cylindrical Combustor," AIAA Paper 2013-3966, 2013. https://doi.org/10.2514/6.2013-3966

[40] Kobald, M., Ciezki, H., and Schlechtriem, S., "Optical Investigation of the Combustion Process in Paraffin-Based Hybrid Rocket Fuels," AIAA Paper 2013-3894, 2013. https://doi.org/10.2514/6.2013-3894

[41] Kobald, M., Verri, I., and Schlechtriem, S., "Theoretical and Experimental Analysis of Liquid Layer Instability in Hybrid Rocket Engines," *CEAS Space Journal*, Vol. 7, No. 1, 2015, pp. 11–22. https://doi.org/10.1007/s12567-015-0076-2

[42] Kobald, M., Petrarolo, A., and Schlechtriem, S., "Combustion Visualization and Characterization of Liquefying Hybrid Rocket Fuels," AIAA Paper 2015-4137, 2015. https://doi.org/10.2514/6.2015-4137

[43] Petrarolo, A., Kobald, M., and Schlechtriem, S., "Liquid Layer Combustion Visualization of Paraffin-Based Hybrid Rocket Fuels," AIAA Paper 2017-4828, 2017. https://doi.org/10.2514/6.2017-4828

J. M. Seitzman
Associate Editor